Neurobiology of Aging 107 (2021) 96–108

Contents lists available at ScienceDirect

Neurobiology of Aging

journal homepage: www.elsevier.com/locate/neuaging.org

Vascular endothelial growth factor associated dissimilar cerebrovascular phenotypes in two different mouse models of Alzheimer's Disease

Nicholas M. Tataryn[a,b,f,1], Vishal Singh[c,1], Jonathan P. Dyke[d], Hanna E. Berk-Rauch[b], Dana M. Clausen[c], Eric Aronowitz[d], Erin H. Norris[b], Sidney Strickland[b], Hyung Jin Ahn[c,e,*]

[a] *Tri-Institutional Training Program in Laboratory Animal Medicine and Science, Memorial Sloan Kettering Cancer Center, Weill Cornell Medicine, and The Rockefeller University, New York, New York, USA and Center for Comparative Medicine and Pathology, Memorial Sloan Kettering Cancer Center, New York, NY, USA*

[b] *Patricia and John Rosenwald Laboratory of Neurobiology and Genetics, Rockefeller University, New York, NY, USA*

[c] *Department of Pharmacology, Physiology and Neurosciences, Rutgers-New Jersey Medical School, Newark, NJ, USA*

[d] *Citigroup Biomedical Imaging Center, Department of Radiology, Weill Cornell Medicine, New York, NY, USA*

[e] *Brain Health Institute, Rutgers University, Piscataway, NJ, USA*

[f] *Division of Comparative Medicine, Vanderbilt University Medical Center, Nashville, TN, USA*

ARTICLE INFO

Article history:
Received 16 February 2021
Revised 15 July 2021
Accepted 20 July 2021
Available online 28 July 2021

Keywords:
Alzheimer disease
Arterial spin labeling (ASL)
Cerebral blood flow
Cerebral blood volume
Vascular endothelial growth factor
Cerebral metabolism
Dynamic susceptibility contrast-enhanced magnetic resonance imaging

ABSTRACT

Vascular perturbations and cerebral hypometabolism are emerging as important components of Alzheimer's disease (AD). While various *in vivo* imaging modalities have been designed to detect changes of cerebral perfusion and metabolism in AD patients and animal models, study results were often heterogenous with respect to imaging techniques and animal models. We therefore evaluated cerebral perfusion and glucose metabolism of two popular transgenic AD mouse strains, TgCRND8 and 5xFAD, at 7 and 12 months-of-age under identical conditions and analyzed possible molecular mechanisms underlying heterogeneous cerebrovascular phenotypes. Results revealed disparate findings in these two strains, displaying important aspects of AD progression. TgCRND8 mice showed significantly decreased cerebral blood flow and glucose metabolism with unchanged cerebral blood volume (CBV) at 12 months-of-age whereas 5xFAD mice showed unaltered glucose metabolism with significant increase in CBV at 12 months-of-age and a biphasic pattern of early hypoperfusion followed by a rebound to normal cerebral blood flow in late disease. Finally, immunoblotting assays suggested that VEGF dependent vascular tone change may restore normoperfusion and increase CBV in 5xFAD.

1. Introduction

Increasing evidence suggests that vascular perturbations are a potential driver of neuronal degeneration and cognitive decline in Alzheimer's disease (AD) (de la Torre, 2004; Ostergaard et al., 2013; Zlokovic, 2011). For instance, there is a well-established association between cerebral hypoperfusion and memory impairment as the disease progresses (Austin et al., 2011; Sierra-Marcos, 2017). The most profound hypoperfusion occurs in areas that are known to be sites of early plaque accumulation and those that control memory storage and retrieval, drawing a link between vascular perturbations and the primary symptoms of the disease. Furthermore, the brains of AD patients are less able to increase blood flow in response to neural activity (neurovascular coupling) (Girouard and Iadecola, 2006; Iadecola, 2004), causing already affected areas to be deprived of blood flow when attempting critical tasks. In addition to having vascular abnormalities as the result of the disease, there is also evidence that vascular disturbances such as those encountered with hypertension and diabetes could play a role in the cause or progression of AD (Viswanathan et al., 2009). Whether cause, effect, or some combination of both, there is a clear association between altered cerebrovascular function and disease progression in AD. In addition to hypoperfusion, AD patients also frequently show decreased cerebral metabolism as the disease progresses (Herholz et al., 2011). The decrease in cerebral metabolism may be a consequence of decreased perfusion as reduced blood delivery would entail lower glucose availability. While the exact

* Corresponding author at: Department of Pharmacology, Physiology and Neurosciences, Rutgers-New Jersey Medical School, Newark, NJ, USA, 1-973-972-6614.
E-mail address: hyungjin.ahn@rutgers.edu (H.J. Ahn).

[1] Nicholas M. Tataryn and Vishal Singh equally contributed to this work

0197-4580/$ – see front matter
https://doi.org/10.1016/j.neurobiolaging.2021.07.015

mechanisms of hypometabolism are still under investigation, there is a clearly consistent pattern of decreased glucose uptake in AD patients.

In order to aid in diagnosis of AD, noninvasive imaging technologies have been employed to detect hemodynamic abnormalities and hypometabolism. Recent advances in such neuroimaging techniques have contributed greatly to earlier and more reliable detection in AD patients (Montagne et al., 2016). Of the two classical pathologies, in vivo amyloid imaging has become well established, with tau imaging also showing promising recent developments (Brosch et al., 2017; Chandra et al., 2019). Methods originally developed to assess blood flow in ischemic or traumatic brain injury have also been adapted for the diagnosis of AD. Imaging techniques commonly employ magnetic resonance imaging (MRI) or positron emission tomography (PET) to investigate aspects of blood flow, metabolism, or amyloid and tau accumulation that have been observed to change throughout the course of the disease. For example, arterial spin labeling (ASL) MRI and ^{18}F-Fluorodeoxyglucose positron emission tomography (FDG-PET) have revealed that patients with AD show decreased perfusion and cerebral glucose metabolism compared to non-demented control subjects (Chen et al., 2011; Du et al., 2006). Furthermore, hypometabolism of specific regions can be seen in clinical as well as presymptomatic AD patients (Mosconi et al., 2010), making FDG-PET a valuable tool for early diagnosis. As a result of continued positive findings, noninvasive imaging has become more widely adopted as an early diagnostic tool in AD. PET imaging is commonly employed to complement behavioral testing in diagnosis of early AD and mild cognitive impairment, with FDG and amyloid targeting tracers used most commonly (Caminiti et al., 2018; Kato et al., 2016; Rice and Bisdas, 2017).

Considering the clinical and diagnostic significance of neurovascular and metabolic abnormalities in human AD patients, it is crucial to understand if animal models of AD display similar characteristics and if separate models vary in regard to these modalities. Transgenic murine models of AD have long been the mainstay for early and preclinical AD research. These mice usually contain mutated human copies of genes for amyloid-β precursor protein (APP), presenilin (PS1 or PS2), or some combination thereof. These mutations lead to cerebral amyloid deposition and result in effects that resemble what is observed in human AD, such as cognitive decline, inflammation, and neurodegeneration (Hall and Roberson, 2012).

Various imaging modalities have been previously employed in AD mice and have yielded assorted and sometimes contradictory results (Deleye et al., 2016; Dubois et al., 2010; Hebert et al., 2013; Klohs et al., 2014; Macdonald et al., 2014; Rojas et al., 2013; Waldron et al., 2015; Xiao et al., 2015). Findings have included hypoperfusion, atrophy of the hippocampus and cortex, hypometabolism and hypermetabolism. It can be difficult to interpret or compare experiments that are conducted by separate researchers because these studies are often heterogeneous with respect to imaging procedures, anesthetic protocols, handling conditions, data acquisition, or image analysis. It is also often assumed that different AD mouse strains will show similar pathology, which entails that finding in one strain may guide future studies in another. We set out to test these assumptions by performing imaging studies in two AD mouse strains under identical conditions, focusing primarily on aspects of cerebral blood flow and metabolism. The two strains used were TgCRND8 and 5xFAD, which were selected for specific differences in inserted genes and predominant type of Aβ, which may result in different cerebrovascular phenotypes. Specifically, 5xFAD miceharbor presenilin mutations (in addition to APP mutations) and accumulate predominantly Aβ_{42}, whereas TgCRND8 mice carry only APP mutations, resulting in accumulation of a more heterogeneous amyloid pool with the majority being Aβ_{40} (Van Vickle et al., 2007). These mice are also reported to exhibit different rates of disease progression, with 5xFAD mice showing earlier amyloid deposition and more rapid disease course along with neuronal cell loss, which is not prevalent in TgCRND8 mice (Oakley et al., 2006).

We used three in vivo imaging modalities including ASL-MRI, dynamic susceptibility contrast-enhanced magnetic resonance imaging (DSC-MRI), and FDG-PET. These methods are meant to measure cerebral blood flow (CBF), cerebral blood volume (CBV), and cerebral metabolism, respectively. In addition to characterizing the cerebrovascular phenotype of these mice, these imaging modalities were also evaluated for their ability to monitor disease progression in AD mice. We have also investigated the molecular mechanism behind alteration in perfusion in these two strains focusing on neuroinflammation and vascular tone.

2. Materials and methods

2.1. Mice

Two strains of mice were used. All genotypes were determined by PCR analysis of tissues collected for identification purposes. Genotypes were confirmed again following euthanasia. TgCRND8 mice were bred and maintained at our institution with breeding progenitors acquired from the University of Toronto (Chishti et al., 2001). TgCRND8 mice are transgenic for the human APP695 gene with Swedish and Indiana mutations driven by the prion promoter, PrP. These mice develop amyloid deposition by 3 months-of-age and show vascular amyloid deposition by 6 months. Pathological findings are accompanied by cognitive deficits detectable at 3 months-of-age and more pronounced at 6 months. 5xFAD mice were also bred in house with breeding progenitors purchased from The Jackson Laboratory (Bar Harbor, ME). These mice, also known as 5xFAD mice, are transgenic for two genes with a total of five familial AD mutations (Oakley et al., 2006). Inserted genes include the human APP695 with Swedish, London, and Florida mutations as well as a human PSEN1 gene with M146L and L286V mutations. Each gene is driven independently by a mouse Thy-1 promoter. 5xFAD mice show amyloid deposition by 2 months. Cognitive deficits are detectable at 4–6 months. Cerebral Aβ42 levels began rising at 1.5 months in 5xFAD mice, in both males and females (brain Aβ42 levels were ~0.3–0.7 ng/mg protein). There is also a rise in Aβ40 levels of both male and female 5xFAD mice around 2 months of age (Oakley et al., 2006). Young female 5xFAD mice are reported to have slightly higher Aβ42 levels than age-matched males, but this trend appears to diminish at older ages (Oakley et al., 2006). Aβ plaque onset in TgCRND8 occurs at 3 months of age in both male and female mice and there is no significant difference in levels based on gender. Aβ42 levels in TgCRND8 mice were 4,600 $\pm$ 1,560 pmol/g of brain while Aβ40 levels were 2,440 $\pm$ 350 pmol/g of brain (Chishti et al., 2001).

Primary studies employed female mice of both strains. In order to minimize effects of the estrus cycle, mice were co-housed in groups of three to five animals, which has been shown to suppress and synchronize estrus (Lee S. van der, 1956). All groups of transgenic (AD) mice were compared to wild type (WT) littermate controls in the study. Mice were divided into two age groups for each strain: the younger group was approximately 7 months (range 6.3–7.4 months) and the older group was approximately 12 months (range 12.1–13.1 months). These ages were chosen as representative of early (but readily detectable) disease and late disease stages. All mice were maintained in a vivarium accredited by AAALAC International, and all activities were approved

by Institutional Animal Care and Use Committees at The Rockefeller University or Weill Cornell Medicine. All husbandry, experiments, and animal handling were conducted in accordance with the Public Health Service Policy (1986) and The Guide for the Care and Use of Laboratory Animals. All findings are reported in accordance with the ARRIVE guidelines. Mice were specific-pathogen-free and were housed in solid-bottom, polysulfone caging with autoclaved corn cob bedding. Mice were provided gamma-irradiated feed (LabDiet 5053, PMI, St Louis, MO) and acidified water (pH 2.5–2.8) ad libitum. The holding area was ventilated with 100% HEPA-filtered outside air at 10–15 air changes hourly. Temperature was 72+/-2°F (21.5 +/- 1°C), relative humidity 30%–70%, and there was a 12:12-hours light:dark photoperiod. Imaging studies were conducted during the light phase between times 1000 and 1700.

2.2. Arterial spin labeling

ASL is an MRI-based technique which uses radio frequency pulses to label water molecules within the vasculature, thereby using the blood as an endogenous tracer in order to quantitatively assess blood flow to a particular tissue of interest (Petcharunpaisan et al., 2010). ASL has been employed in human AD patients to show a rather consistent pattern of decreased cerebral perfusion that worsens with disease progression (Chao et al., 2010; Du et al., 2006).

All MRI images were obtained using a 7.0 Tesla 70/30 Bruker Biospec small animal imaging system (Bruker Biospin, Ettlingen, Germany) with 450 mT/m gradient amplitude and a 4500 T/m/s slew rate. A volume coil was used for transmission and a surface coil for reception. Mice were anesthetized using isoflurane (2%–4% in 100% oxygen) and anesthesia was also maintained with isoflurane (1%–3% in 100% oxygen). Animals were warmed using a warm water recirculating unit. Throughout the imaging procedure, respirations were monitored using an inflatable transmitter pad placed beneath the thoracic region of the mouse. Isoflurane was adjusted to keep respiratory rate within a narrow range with the target of 60–70 breaths per minute in order to maintain a consistent depth of anesthesia between groups. Anatomical scans were performed using T_2 weighted images and these images were later used to guide region of interest (ROI) construction. Anatomical images were also used to locate a transversal slice at approximately Bregma 0.50 mm (Paxinos and Franklin, 2004). This position was used for subsequent ASL imaging, which was based on a pulsed ASL FAIR-RARE pulse sequence labeling the inflowing blood by global inversion of the equilibrium magnetization (Kim, 1995a). The difference of the labeled and unlabeled images then yields a measure of the relative CBF (Herscovitch and Raichle, 1985; Kim, 1995b). Two axial slices were acquired with a field of view of 15 × 15 mm, spatial resolution of 0.117 × 0.117 × 1 mm, TE of 5.37 ms, effective TE of 48.32 ms, recovery time of 10 s, and a RARE factor of 72 resulting in a total scan time for the rCBF images of ∼48 min. The two slices were averaged to yield a single image for analysis. Individual slices were also evaluated and showed similar results, so averaged slices were used for simplicity of reporting. The locations of slices analyzed were chosen for their clear delineation of cortex, hippocampus, and thalamus, which are known areas of amyloid accumulation in these mice.

For computation of rCBF, the Bruker ASL perfusion macro was used. It uses the model of Kober (Kober et al., 2004) and includes steps to mask background signal and ventricles. The ASL sequence was found to give suitable measures of CBF when validated with radioactive microsphere PET (Bos et al., 2012). The images were exported to Analyze format on the MRI console and further processed using NIH-developed ImageJ software (Bethesda, MD). For all image analysis, ROIs were drawn manually such that the entire ROI was safely contained within the brain area of interest, mitigating motion artifacts and resolution limitations that can distort data at the borders of these areas. ROIs were drawn separately but isometrically for each cerebral hemisphere to avoid effects of large central vessels. Average values for each hemisphere were combined and output data were recorded as mL/100g/min.

2.3. Dynamic susceptibility contrast-enhanced magnetic resonance imaging

In order to determine if perfusion differences were due to changes in CBV, dynamic susceptibility contrast-enhanced MRI (DSC-MRI) was employed. DSC-MRI uses an injected contrast agent such as gadolinium-diethylenetriamine pentaacetic acid (Gd-DTPA) as a blood tracer. When detected in the brain, increased contrast will result in signal attenuation which can be quantified to estimate the relative concentration of contrast present, which is then used to calculate CBV. Because AD mice have been reported to have changes in the blood-brain barrier, CBV was corrected for permeability differences according to the equations of Boxerman-Weisskoff.(Boxerman et al., 2006). Images were acquired using the same MRI equipment as above for ASL. A 26G intravenous catheter was placed in the lateral tail vein for contrast injection. Following catheterization, mice were anesthetized using isoflurane (2%–4% in 100% oxygen) and anesthesia was maintained with isoflurane (1%–3% in 100% oxygen).

MRI signal was acquired from every voxel in the image at 3.9 sec intervals over a period of 3 minutes to monitor for increased signal enhancement from injected contrast. A FLASH sequence was used with TR of 41.5 ms and TE of 2.9 ms and a 20-degree flip angle. The brain was split into five slices with slice thickness of 1.25 mm and 0.25 mm gap between slices. The middle (third) slice was used for analysis and corresponded with the region analyzed by ASL. Each image yielded a 128 × 128 matrix with 25 x 25 mm field of view. Following a 30 second baseline period, MRI contrast (Gd-DTPA; 15 μmol) was injected intravenously over 10 seconds while images were continuously acquired. Images were exported to Analyze format and further processed using ImageJ software. ROIs were constructed in a similar manner to those for ASL. Images were analyzed using the DSCoMAN plugin for ImageJ (DP Barboriak Lab, Duke University). This program uses the equations of Boxerman and Weisskoff (Boxerman et al., 2006) to compute corrected CBV values. Scans were included from the time the MRI signal saturated (second scan, at 7.8 seconds) until the end of the scan (314.5 seconds) with baseline values during the interval from 7.8s to 19.9s.

2.4. [^{18}F]-Fluorodeoxyglucose positron emission tomography

^{18}F-Fluorodeoxyglucose (FDG), a radiolabeled glucose analogue, was used in PET to assess glucose metabolism in the brains of AD mice (Sarikaya, 2015). When used in imaging of the brain, it has proven to be a valuable clinical tool for detecting decreases in cerebral metabolism that are seen in AD patients (Garibotto et al., 2017; Ng et al., 2017). Scans were performed using an Inveon micro PET/CT system (Siemens Medical Solutions, Knoxville, TN, USA). It has been shown that when mice are anesthetized during the FDG uptake period, FDG activity in the brain is greater when no fasting occurs (Fueger et al., 2006). In the current study, food was removed from the cage approximately 1hr prior to radionuclide injection to prevent recently ingested food from interfering with cerebral metabolism of FDG. Mice were injected intravenously with [^{18}F]-FDG via the lateral tail vein followed by a

20–30 minutes uptake period. Mice were anesthetized during the uptake period using isoflurane (2%–4% in 100% oxygen). CT projections (120 views in half rotation) were acquired for attenuation correction and anatomic landmarks. The X-ray tube settings were 80 kVp and 500 μA. The resulting raw data were reconstructed into a final image matrix of 1024 × 1024 × 480 slices at 98-μm voxel size. PET Data were then acquired for 60 minutes into 6 × 10 minutes frames while mice remained under isoflurane anesthesia (2% in 100% oxygen). This period was chosen because it has been shown to capture the plateau in brain uptake following intravenous FDG injection (Fueger et al., 2006; Luo et al., 2012). Mice were warmed throughout the imaging procedure using a heat lamp placed approximately 16 inches from the front opening of the bore.

Sinograms were reconstructed into 128 × 128 matrix with 0.78 x 0.78 x 0.8 mm voxel size using OSEM 3D/MAP (2 OSEM and 18 MAP iterations). The reconstructed images were viewed and analyzed using the Inveon Research Workspace software (Mercury Computer Systems, Inc., Chelmsford, MA, USA). Standardized uptake value (SUV) measurements were used to correct for exact dosage and mouse weight. ROIs were constructed in three dimensions in a manner similar to those of ASL and DSC-MRI. In our studies and in others, (Hebert et al., 2013) analysis of numerous regions of the mouse brain typically show similar relationships. Therefore, for simplicity of reporting, only values for whole brain measurements are presented although regional measurements showed similar outcomes in all groups. Whole brain ROIs were drawn manually using the overlaid CT image as reference. Borders were kept safely within the cranial cavity, rostral to the cerebellum and caudal to the olfactory bulbs in order to mitigate potential motion artifacts and to capture regions most affected by amyloid accumulation.

2.5. Immunoblotting

After perfusion and dissection, cortices from the brain of each TgCRND8 and 5xFAD mouse were homogenized in tissue lysis buffer (25 mM Tris, pH 7.4, 2% SDS, 95 mM NaCl, 10 mM EDTA, 1X protease inhibitor cocktail, 1X phosphatase inhibitor cocktail). Total protein concentrations were determined using the Bio-Rad protein assay kit. Equal amounts of proteins were loaded and separated on 10% SDS–PAGE or 4–20%Tris-Glycine Mini Protein Gels (Life Technologies) and then transferred to polyvinylidene fluoride membranes (Millipore). The membranes were then incubated with anti-VEGF (Santa Cruz, 1:1000), anti-VEGF Receptor 2 (Millipore, 1:500), anti-CD31 (Cell Signaling, 1:1000), anti-CD11b (DSHB,1:20), anti-GFAP (Dako, 1:3000), anti-Smooth muscle cell actin (Cell Signaling, 1:1000), or anti-GAPDH (Santa Cruz, 1:20,000) antibodies at 4 °C overnight, followed by incubation with HRP-conjugated secondary antibodies. The proteins were visualized by SuperSignal West Pico Chemiluminescent Substrate (Pierce). The density of bands was normalized to GAPDH and quantified using NIH Image J.

2.6. Statistical analysis

All data are reported as mean +/- standard error (SEM) or percent difference from WT. All error bars represent SEM. All groups of AD mice were compared to WT littermate controls and were analyzed using two-way ANOVA with Bonferroni post-hoc test or a non-paired two tailed student's t-test using GraphPad Prism. For ASL analyses, data are reported as average perfusion value over the constructed ROI. DSC data are reported as corrected regional cerebral blood volume. For FDG-PET studies, the average SUV over the constructed ROI is used for comparison. For all modalities, differences are considered statistically significant when $p < 0.05$. In figures, statistical significance is indicated by asterisks ($^{*} = p < 0.05$; $^{**} = p < 0.01$; $^{***} = p < 0.001$).

3. Results

3.1. Different patterns of regional cerebral blood flow in TgCRND8 and 5xFAD mice

In order to compare CBF in these AD mouse models, ASL was performed at 7 and 12 months-of-age in both strains of mice. For each strain, AD mice were compared to their WT littermate controls. TgCRND8 mice showed no differences in perfusion at 7 months compared to controls (Fig. 1A). At 12 months, there was significant hypoperfusion in both the cortex (-31%; $p < 0.0001$) and the hippocampus (-24%; $p = 0.006$) with no significant change in the thalamus (Fig. 1B). As a pictorial representation of these data, ASL images from each group were overlaid and mathematically averaged using ImageJ software. Averaged scans for each group were set to the same colorimetric scale such that hotter colors (white > yellow > red > blue) represent greater perfusion values (Fig. 1C, D). Anatomic T2 images in Fig. 1E are representative images of coronal slices which were used for perfusion analysis and construction of ROIs. Taken together, these data indicate an age-related decrease in cerebral perfusion in TgCRND8 mice that is apparent by 12 months-of-age but not yet at 7 months.

In contrast, 5xFAD mice showed a biphasic response in CBF with hypoperfusion at 7 months followed by a rebound to normoperfusion by 12 months. At 7 months, there was a significant decrease in the cortex (-33%; $p = 0.012$) with non-significant changes in other regions (Fig. 2A). At 12 months-of-age, 5xFAD mice showed no significant difference compared to their WT littermate controls (Fig. 2B). It appears from these results that early hypoperfusion yields to a later rebound in normal perfusion. Averaged scans for each group were set to the same colorimetric scale as 5xFAD mice (Fig. 2C, D). These images clearly show hypoperfusion in the cortex of 7-month-old 5xFAD (Fig. 2A) but normal perfusion in 12-month-old 5xFAD mice (Fig. 2B) compared to their WT littermate controls.

3.2. Increased cerebral blood volume in 5xFAD mice

DSC-MRI was used in the same age groups of both strains in order to determine if there were any changes in CBV and values were calculated using the equations of Boxerman and Weisskoff (Boxerman et al., 2006). TgCRND8 mice showed no significant differences at both 7 and 12 months-of-age compared to WT littermate controls (Fig. 3A, B). 7-month-old 5xFAD mice showed a significant increase in CBV in only the hippocampus (+157%; $p = 0.019$; Fig. 3C) compared to controls. At 12 months-of-age, AD mice showed even more drastic increases in CBV with significant increases in the hippocampus (+247%; $p = 0.018$) and thalamus (+149%; $p = 0.0012$) and a strong tendency of increase in the cortex ($p = 0.08$) (Fig. 3D).

DSC data are presented pictorially in Fig. 3E. For these scans, images from each group were overlaid and mathematically averaged using ImageJ software. In each group, the average images for WT mice were mathematically subtracted from those of their AD counterparts, resulting in a single image showing the difference in volume between the groups. These were then set to the same colorimetric scale designed to show positive values (increased CBV in AD) as red and negative values (decreased CBV in AD) as blue. Altogether, TgCRND8 mice showed no significant differences in CBV while 5xFAD mice showed a reliable pattern of increased CBV that became more severe and widespread with age. DSC data are also displayed as time curves in Fig. 4, which demonstrates qualitative

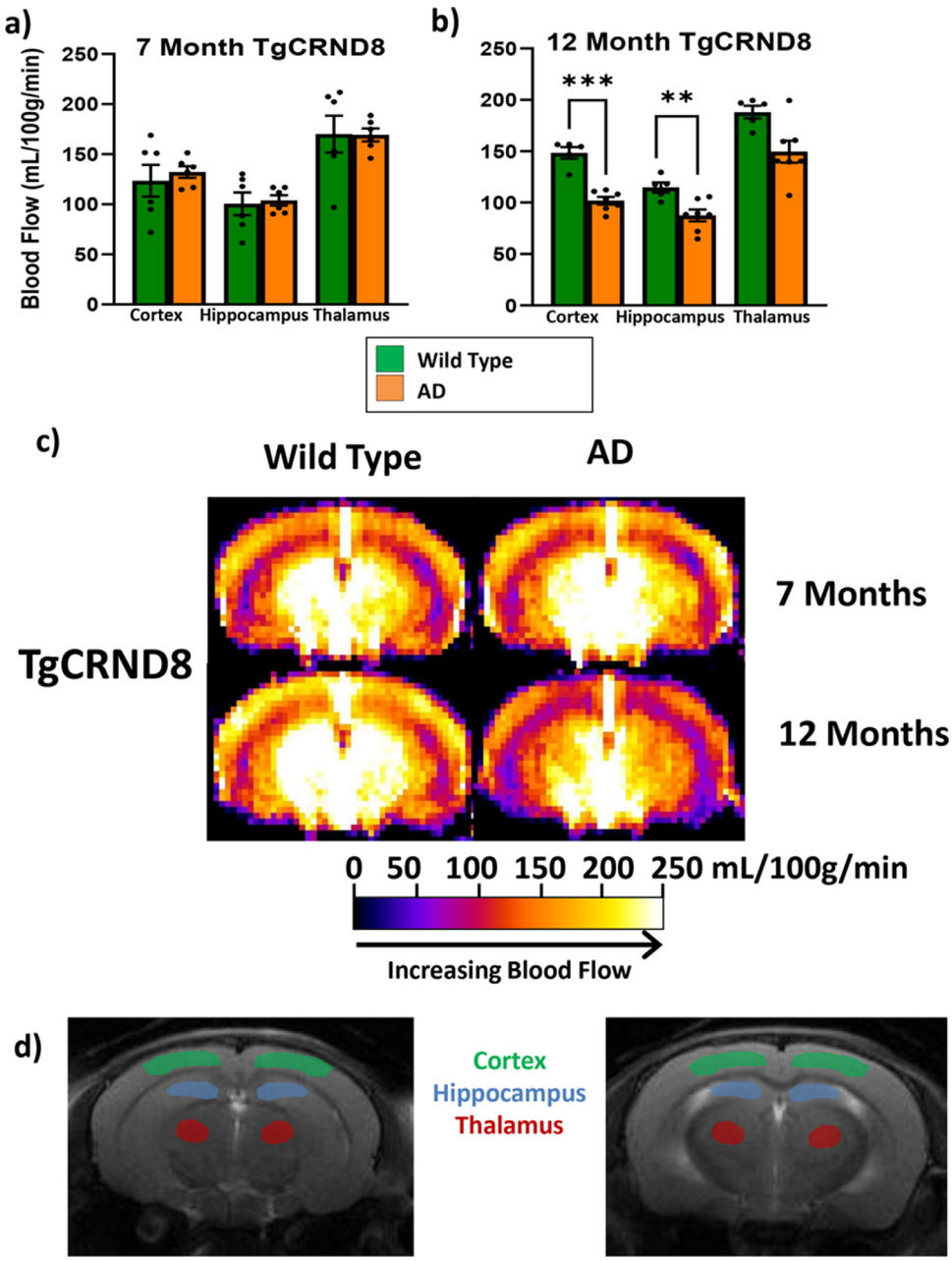

Fig. 1. TgCRND8 mice show progressive cerebral hypoperfusion by arterial spin labeling (ASL). Bar graphs represent average perfusion values for respective regions of interest – cortex, hippocampus, and thalamus. TgCRND8 mice showed no changes at 7 mo (A) n = 6 WT, 6 AD, not significant) but decreased perfusion at 12 mo (B) n = 5 WT, 7 AD). Decreases were found in the cortex ($^{***}p < 0.001$) and hippocampus ($^{**}p < 0.01$). Visual presentations of this data were created using ASL images with increased perfusion values indicated by warmer colors (red, orange, yellow, white) and lesser values represented by colder colors (blue, purple; (C). T2 weighted MRI scans were used for anatomical reference of key brain regions (D). Conservative ROIs were chosen to reduce edge effects from the brain surface, ventricles, and large midline vessels. Representative ROIs are shown. Statistical analyses were performed using two-way ANOVA with Bonferroni post-hoc test. "(For interpretation of the references to color in this figure legend, the reader is referred to the Web version of this article.)"

kinetic differences between groups. Relative CBV was estimated from signal enhancement using the equation $-\ln(S/S_0)TE$, where S_0 is the baseline signal, prior to Gd-DTPA injection, and TE is the echo time. The cortex was used as a representative brain region while other regions showed similar trends. TgCRND8 mice showed similar curves at both 7 and 12 months-of-age compared to WT littermate controls (Fig. 5A, B), whereas 5xFAD mice showed increased signal enhancement with a protracted time course compared to WT littermate controls (Fig. 5C and D). These results show that there is a clear increase in the area under the curve for 5xFAD mice at both ages, which represents increased CBV. There is no such increase observed in TgCRND8 mice. This result supports the conclusions from quantitative analyses using the equations of Boxerman and Weisskoff.

3.3. Cerebral hypometabolism in aged TgCRND8 mice

To assess cerebral glucose metabolism in AD mice, we performed FDG-PET in both strains at 7 and 12 months-of-age. This imaging modality served as a measure of metabolic activity in the brain, as changes result in corresponding alterations in FDG uptake values. In TgCRND8 mice at 7 months, there were no sig-

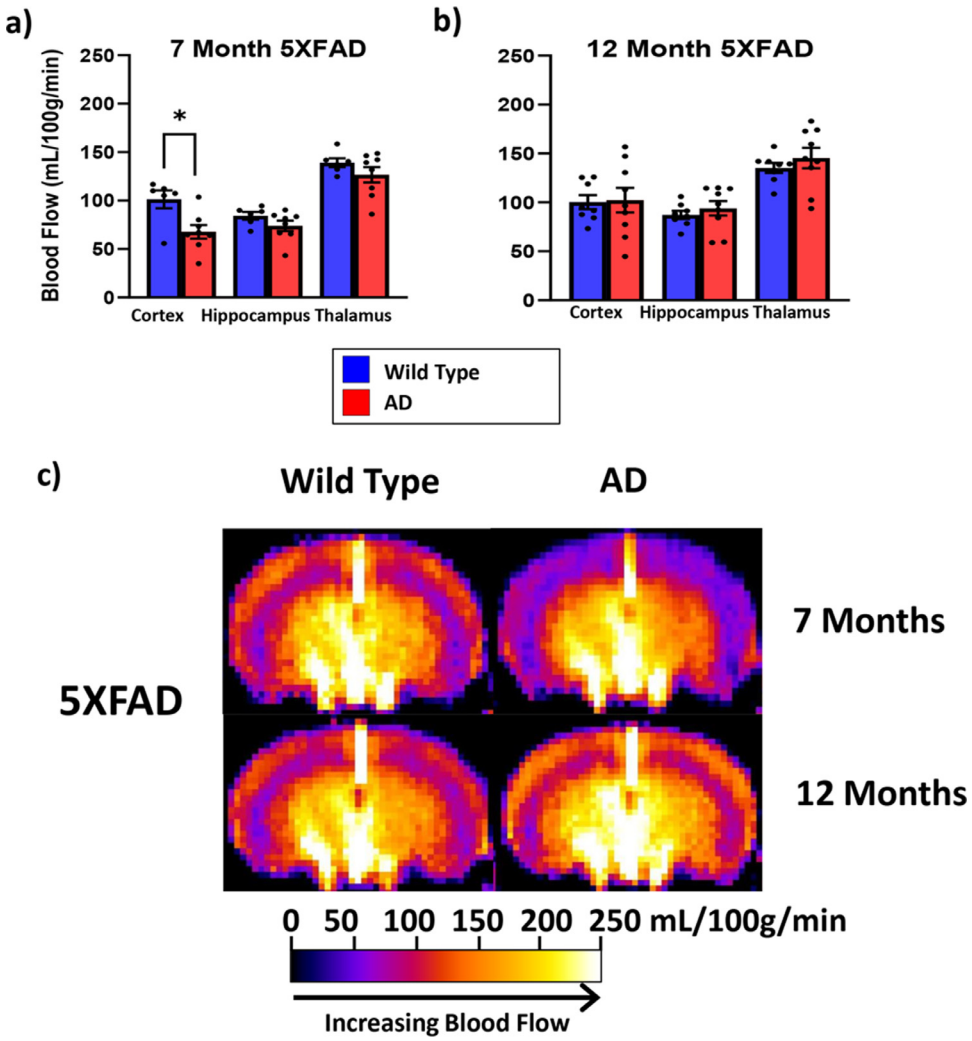

Fig. 2. 5xFAD mice show a biphasic pattern of cerebral blood flow by ASL. 5xFAD mice showed a significant decrease of perfusion in the cortex at 7 mo (A) n = 6 WT, 8 AD; $^{*}p < 0.05$) followed by a rebound to normoperfusion at 12 mo with a slight trend toward hyperperfusion (B) n = 8 WT, 9 AD, not significant). Visual representations of ASL data are presented with the same colorimetric scale as that used in Fig. 1 (C) with increased perfusion values indicated by warmer colors (red, orange, yellow, white) and lesser values are represented by colder colors (blue, purple). "(For interpretation of the references to color in this figure legend, the reader is referred to the Web version of this article.)"

nificant differences (Fig. 5A). In older TgCRND8 mice, there was a substantial decrease in uptake (-25.2%) which was statistically significant ($p = 0.04$; Fig. 5B), suggesting decreased cerebral glucose metabolism in this strain as the disease progresses. On the other hand, 5xFAD mice showed no significant differences at either 7 months (Fig. 5C) or 12 months (Fig. 5D). Sagittal sections of representative mice are presented with color-coded uptake maps for visualization of results in the 12-month age group (Fig. 5E). Hotter colors (red, orange, white) represent higher values while colder colors (blue, purple) represent lower values. The cerebrometabolic results parallel those of the ASL studies in which TgCRND8 mice showed decreased values over time whereas 5xFAD mice appear to retain similar cerebral metabolism compared to WT littermates.

3.4. Vascular endothelial growth factor (VEGF) signaling as a possible mechanism underlying heterogeneous cerebrovascular phenotypes in two AD mouse models

Our MRI and PET imaging results showed that there is clear discrepancy in cerebral perfusion and glucose metabolism between 5xFAD and TgCRND8 mice, especially at 12 months-of-age. We therefore analyzed possible molecular mechanisms underlying heterogeneous cerebrovascular and metabolic phenotypes in these two AD mouse models, focusing on cerebrovascular and neuroinflammatory elements. Since VEGF signaling modulates angiogenesis and vascular tone, and is also associated with the clinical manifestation of AD (Carmeliet, 2005; Mahoney et al., 2021; Maia et al., 2005; Rissanen et al., 2005), we analyzed protein expression levels of VEGF and VEGFR2 in the cortex of 5xFAD and TgCRND8 mice at 12 months-of-age using western blotting analysis and found that both VEGF and VEGFR2 expression are significantly higher in 5xFAD AD mice as compared to WT littermates (Fig. 6A, B). However, there was no significant change in TgCRND8 (Fig. 6A, B). We found a similar pattern of VEGF protein expression using immunohistochemical analysis (Supplementary Fig. 1A).

We measured levels of vascular proteins by western blot analysis and immunohistochemistry to detect any changes in angiogenesis or vascular cell levels in the cortex of both strains. We used CD31 as an endothelial cell marker (Fig. 6C), collagen type IV as a blood vessel marker (Supplementary Fig. 1B) and smooth muscle cell actin (SMCA) (Fig. 6D and supplementary Fig. 1C).

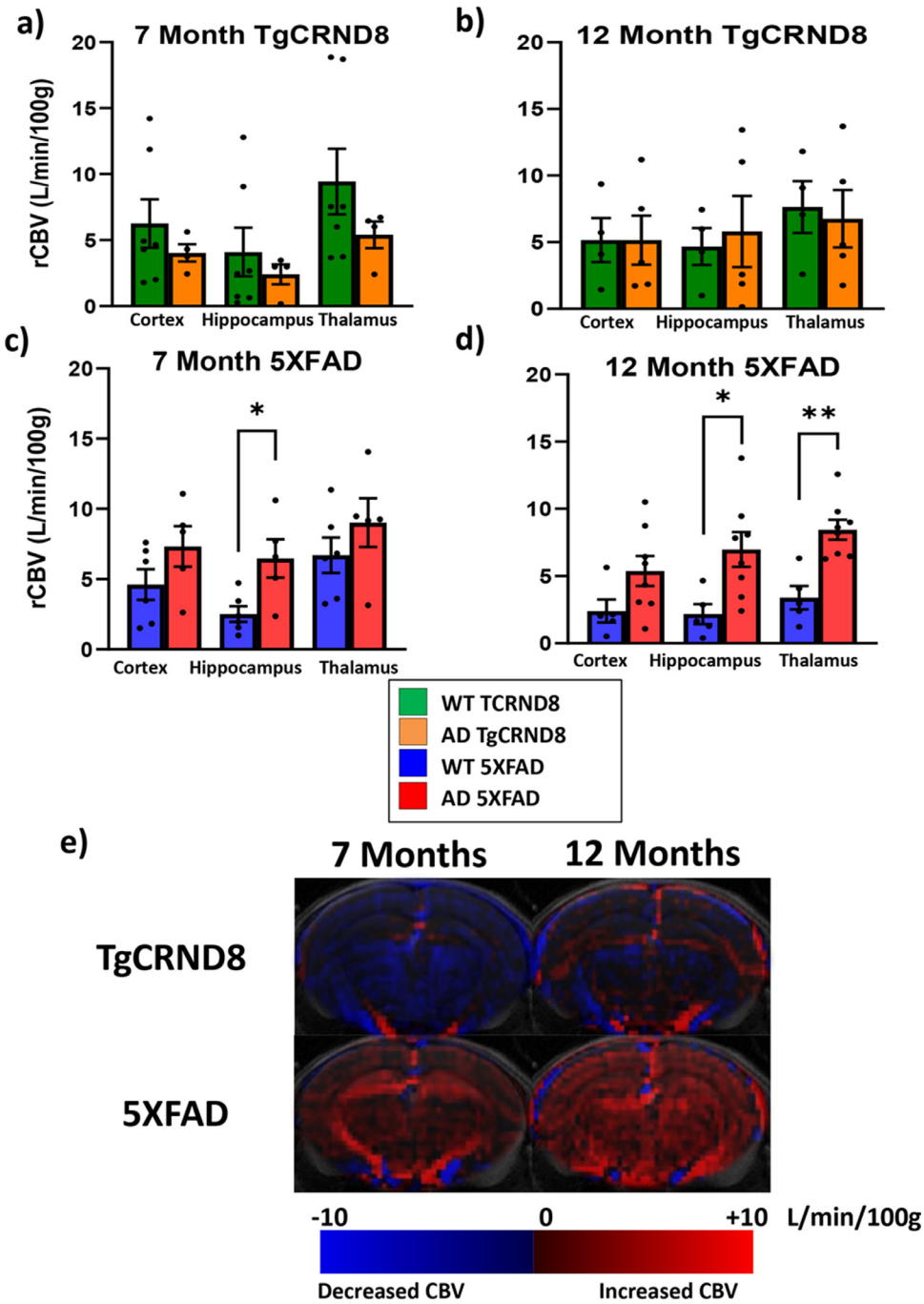

Fig. 3. DSC-MRI shows increased CBV in 5xFAD mice, but not TgCRND8 mice. Bar graphs represent averaged corrected CBV values for each group for respective ROIs. TgCRND8 mice showed no statistical difference at either age but did show a trend toward hypovolemia at 7 mo (A) n = 7 WT, 4 AD; $p \geq 0.35$) which disappeared by 12 mo (B) n = 4 WT, 5 AD). In contrast, 5xFAD mice showed increased CBV at 7 mo (C) n = 6 WT, 5 AD), which was significant in the hippocampus (+157%; $^{*}p < 0.05$). CBV continued to increase and by 12 mo was greater in all areas (D) n = 5WT, 8AD) with significant increases in the hippocampus (+247%; $^{*}p < 0.05$) and thalamus (+149%; $^{**}p < 0.01$). For whole brain visualization of DSC data, groups were averaged as for ASL, and average WT scans were subtracted from AD so that decreased CBV values are negative and increased values positive (E). A colorimetric scale is used so that increased CBV is red and decreased CBV is blue, with brighter colors representing greater values. Colored CBV maps are superimposed onto T2 MRI scans for anatomic reference. Statistical analyses were performed using two-way ANOVA with Bonferroni post-hoc test. "(For interpretation of the references to color in this figure legend, the reader is referred to the Web version of this article.)"

There was no significant change in CD31, collagen type IV or SMCA protein levels in the cortex of either 5xFAD or TgCRND8 compared to WT littermates (Fig. 6C, D and supplementary Fig. 1B, C). These results suggest that higher levels of VEGF and VEGFR2 may induce vasodilation or altered vascular tone in the cerebral vasculature of 5xFAD mice, but without detectable increased angiogenesis.

Since microglia and astrocytes are the main sources of inflammatory factors in the brain (Ryu and McLarnon, 2008) and their activities are highly correlated with decreased CBF during AD progression (Korte et al., 2020), we analyzed protein levels of CD11b as a marker for activated microglia (Mandrekar-Colucci and Landreth, 2010) and glial fibrillary acidic protein (GFAP) as a marker for reactive astrocytes (Ben Haim et al., 2015) using western blot-

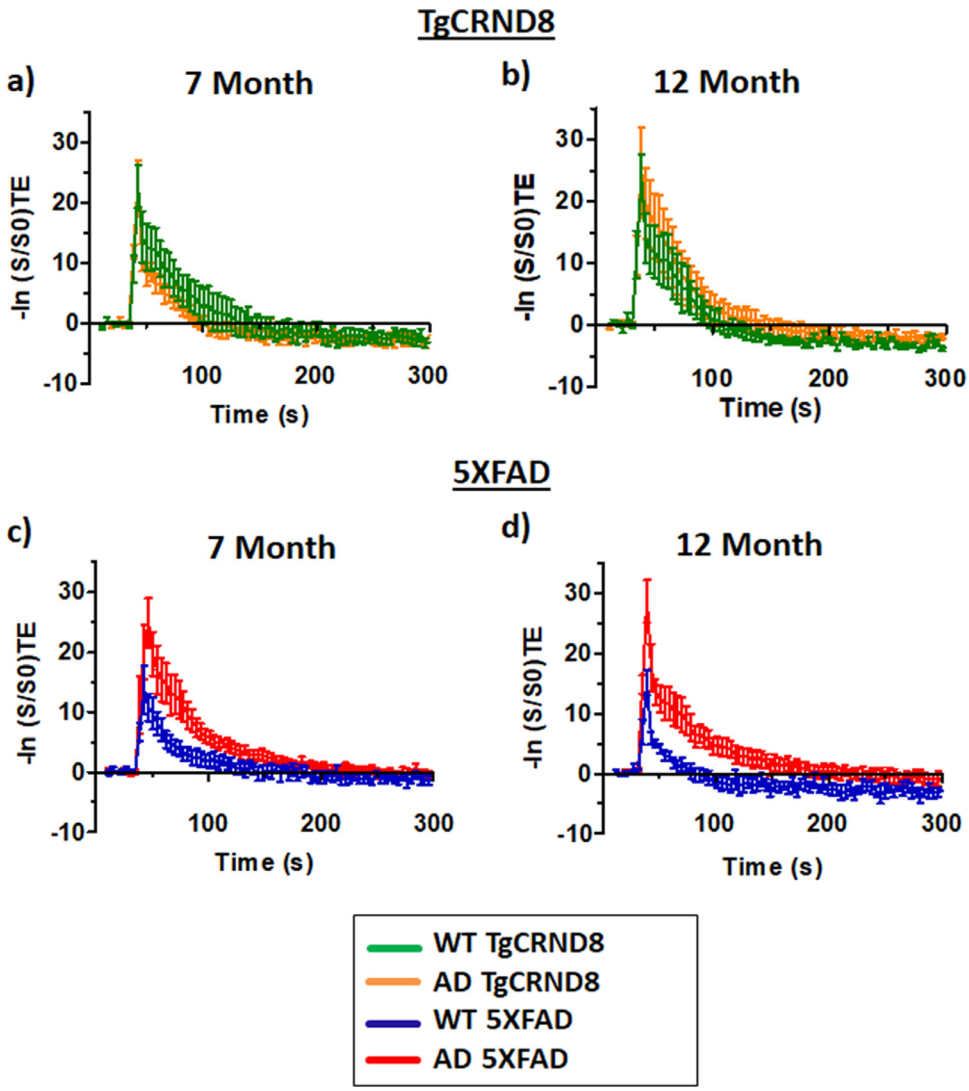

Fig. 4. Kinetic representation of DSC-MRI data. Measurements show relative quantification of signal attenuation to estimate contrast volume in brain regions of interest. Cerebral cortex is presented as a representative region; other regions yielded similar results. In the TgCRND8 strain, AD mice were similar to WT at both ages (A and B). In 5xFAD mice, signal attenuation reached higher peak values and showed more persistent elevation at both ages (C and D). This correlates to contrast volume and provides support to the quantitative data (Fig. 3) which shows increased CBV in 5xFAD mice but not TgCRND8 mice.

ting and immunohistochemical analysis. There were significant increases in levels of CD11b (Fig. 6E and supplementary Fig. 1D) and GFAP (Fig. 6F and supplementary Fig. 1E) compared to WT littermates in the cortex of both 5xFAD and TgCRND8, but no significant difference between 5xFAD and TgCRND8 mice. Overall, these results suggest that activated microglia and reactive astrocytes may be associated with decreased CBF in both TgCRND8 and 5xFAD mice, but increased VEGF signaling may increase CBV and restore normoperfusion in 5xFAD mice. We also analyzed amyloid pathology for 12-month-old 5xFAD and TgCRND8 mice using Cong red staining. This showed that both 5xFAD and TgCRND8 mice have significantly higher amyloid plaque deposition as compared to WT littermates at 12 months of age (supplementary Fig. 1F), but there is no significant difference between 5xFAD and TgCRND8 mice. We also compared GFAP expression and amyloid plaques between 7 and 12-month-old 5xFAD mice, showing no significant difference in GFAP expression or amyloid plaques between these ages (supplementary Fig. 2).

4. Discussion

Our current study reveals interesting insight into the CBF, CBV, and metabolism of two commonly used AD mouse models. Although both 5xFAD and TGCRND8 mice showed the predicted hypoperfusion at some point, there was an interesting restoration of perfusion in 5xFAD mice. Apart from VEGF dependent change, the difference between the two strains may be attributable to a faster, more aggressive disease progression in 5xFAD mice, causing these mice to exhibit hypoperfusion earlier in life, followed by an increase in perfusion and in CBV associated with increases in VEGF/VEGFR. In addition to mutated APP genes, 5xFAD mice express mutant PS1 which leads to preferential accumulation of the highly pathogenic Aβ42. This highly aggressive disease progression may lead to an earlier onset of hypoperfusion which is followed by an increase in CBV and restored perfusion. In TgCRND8 mice, since hypoperfusion occurs later, there may not be evidence of the same compensatory mechanism within the normal lifespan

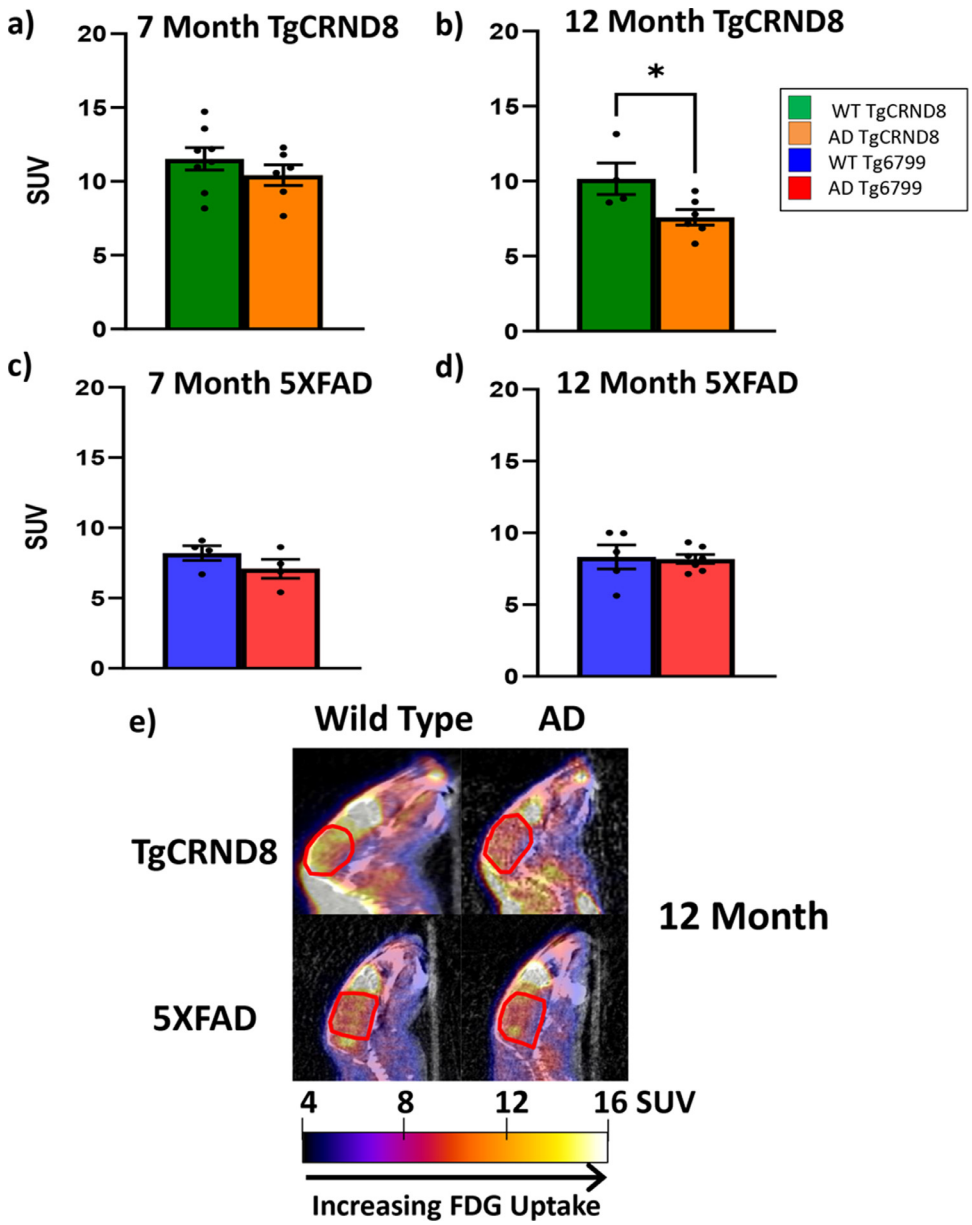

Fig. 5. FDG scans show a discrepancy in cerebrometabolic disease course between strains. TgCRND8 mice showed a slight, non-significant decrease in metabolism at 7 mo (A) n = 7 WT, 6 AD), which further decreased and became statistically significant by 12 mo (B) n = 4 WT, 6 AD; -25.2%; * $p < 0.05$). In contrast, 5xFAD mice showed no statistical difference at either age, but had slightly decreased metabolism at 7 mo (C) n = 4 WT, 4 AD), which nearly disappeared by 12 mo (D) n = 5 WT, 7 AD). Representative scans of individual mice at 12 mo-of-age were set to the same colorimeteric scale (E) with hot colors (red, orange, yellow) representing higher values than cold colors (blue, purple). The measured area (cerebrum) is outlined in red. These scans likewise display decreased FDG activity in TgCRND8 mice but not 5xFAD mice. Statistical analyses were performed using non-paired two tailed student's t-test. All values presented as standardized uptake values (SUV) adjusted for radioactive dose, time, and mouse weight. "(For interpretation of the references to color in this figure legend, the reader is referred to the Web version of this article.)"

of these mice. Although the current study focused on female mice, male mice at 12 months of age showed similar differences in phenotypes (Supplementary Figure 3), suggesting that the discrepancy in cerebrovascular phenotypes is independent of sex.

DSC-MRI also showed distinct patterns between the two strains. TgCRND8 mice showed no significant difference compared to controls whereas 5xFAD mice showed increased CBV that becomes more dramatic and widespread with age. This increased CBV could result from an increase in vascular diameter (vasodilation) or increase in the number of vessels present (increased angiogenesis). However, our immunoblotting results suggest that there is no increase in the number of vascular cells, which would indicate angiogenesis (Fig. 6C, D). Although the increase in VEGF/VEGFR suggests angiogenesis, this could occur alongside vascular reduction such that there is no net change in vascular quantity. Vasodilation or increased vascular compliance is another potential mechanism for the difference between CBV and CBF seen in 5xFAD mice. Whereas ASL employs high temporal resolution to measure nearly instantaneous blood flow, DCE consists of a series of "snap shots" separated by seconds and is more indicative of contrast (blood) volume rather than directly measuring velocity. In 5xFAD mice, there appears to be a close association between increased CBV and a rebound in CBF. In 7-month-old 5xFAD mice, CBV was increased in the hippocampus while CBF was decreased in the cortex. This may represent an early transition period wherein increased CBV is beginning to occur but is unable to compensate for decreased CBF

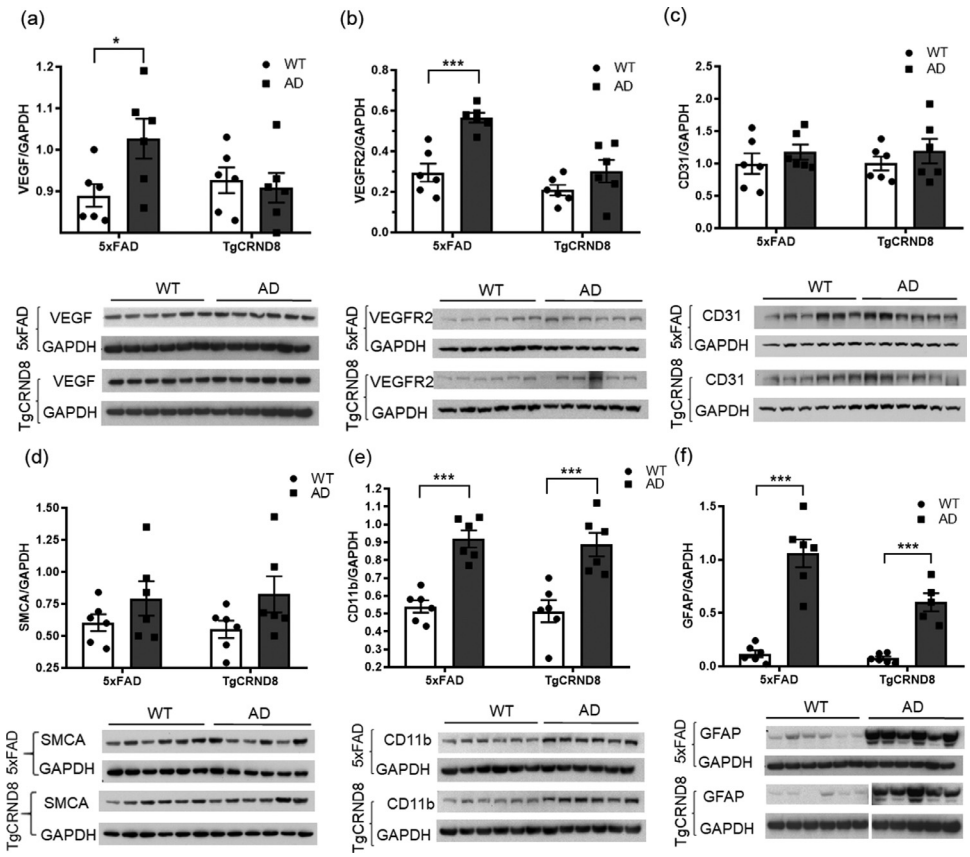

Fig. 6. Immunoblotting assays show significant increase in VEGF signaling with neuroinflammation in 5xFAD and enhanced neuroinflammation in TgCRND8 mice. Immunoblotting was done for various proteins including VEGF (A), VEGFR2 (B), CD31 (C), SMCA (D), CD11b (E) and GFAP (F) in cortical lysate of 5xFAD (n = 6 WT, 6 AD) and TgCRND8 (n = 6 WT, 6 AD). GAPDH was used as loading control. 5xFAD mice showed significant increase in expression of VEGF (A) $^{*}p < 0.05$), VEGFR2 (B) $^{***}p < 0.001$), CD11b (E), $^{***}p < 0.001$) and GFAP (F) $^{***}p < 0.001$) when compared to WT littermates. On the other hand, TgCRND8 mice showed significantly increased expression of CD11b (E), $^{***}p < 0.001$) and GFAP (F) $^{***}p < 0.001$) as compared to WT littermates (n = 5 WT, 5 AD). Statistical analyses were performed using two-way ANOVA with Bonferroni post-hoc test.

until later around 12-month-old. It is therefore possible that cerebral blood vessels are reacting to early decreases in perfusion by increasing vascular compliance, allowing a greater increase in CBF in response to the same systemic blood pressure, and more efficient neurovascular coupling.

In addition to CBF and CBV changes, current experiments also showed predictable decreases in cerebral glucose uptake, but only in older TgCRND8 mice. While the current study showed no differences in 5xFAD mice, previous studies of FDG uptake have been reported in this strain with mixed results. While some studies showed the expected hypometabolism in this strain,(Macdonald et al., 2014; Xiao et al., 2015) others actually showed an increase in uptake.(Rojas et al., 2013) A difference between our findings and previous studies may be due to differences in timing of injections, uptake periods, fasting periods, or image acquisition and analysis. These factors often differ between sites, yielding disparate results. The decreased uptake in TgCRND8 mice likely represents the result of persistent hypoperfusion. As the cerebral tissue becomes less well perfused over time, individual cells are less metabolically active. As for 5xFAD mice, the same mechanism resulting in maintenance of CBF could also account for maintaining cerebrometabolic activity. Amyloid levels may also be predicted to affect cerebral metabolism. Our study showed only12-month-old TgCRND8 mice showed hypometabolism, while both stains showed similar levels of Aβ deposition. However, since 5xFAD mice show an earlier onset of high Aβ deposition, which could result in earlier metabolic effects in this strain that are not observed in TgCRND8 until a more advanced age. In case of AD patients, the association between metabolism and Aβ deposition has been assessed using PET with the amyloid-beta-ligand [(11)C]-labelled Pittsburgh compound-B (PIB) and FDG. Previous studies showed no associations between regional PIB and FDG uptake, indicating that amyloid burden may not correlate with hypometabolism in AD (Altmann et al., 2015; Furst et al., 2012).

VEGF dependent vasodilation leading to change in vascular tone can explain the age dependent restoration of CBF and increase in CBV in 5xFAD. VEGF induces endothelium-dependent relaxation in canine coronary arteries leading to enhanced local blood flow and improved nutrient delivery (Ku et al., 1993). VEGF also has a role in the vascular remodeling and vasodilation that lead to decreased uterine vascular resistance and increased uterine blood flow during pregnancy (Ni et al., 1997). Moreover, VEGF induces endothelium-dependent relaxation in rat aorta (Liu et al., 2001) and causes microvascular relaxation of rat renal arterioles (Maynard et al., 2003). In gliomas, a positive correlation between CBF, CBV and VEGF expression has been reported (Maia et al., 2005). Thus, VEGF dependent changes in vascular tone could be responsible for CBV and CBF alterations in 5xFAD. We observed that increased VEGF and VEGFR2 expression was accompanied with increased CBV and restoration of CBF in cortex of 12 months old 5xFAD mice. However, the CBF restoration and CBV increase in 5xFAD might be not due to VEGF mediated neovascularization since there was no change in CD31 and SMCA expression levels in cerebral blood vessels. Neuroinflammation is an important element of AD and likely

affects cerebrovascular and metabolic findings. Neuroinflammatory events such as extensive gliosis as indicated by marked increased in glial fibrillary acidic protein (GFAP) and CD11b expression, has been reported in AD (Creighton et al., 2019; Hemonnot et al., 2019). It appears from our data that microglial activation and reactive astrocyte do not play a key role, at least in the differences of cerebrovascular phenotypes seen between the two strains, which is our primary focus.

The mechanisms underlying hypoperfusion in AD could be complex and likely multifactorial. Among AD patients, up to 90% suffer from cerebral amyloid angiopathy (CAA) (Chalmers et al., 2003; Ellis et al., 1996), a condition in which amyloid-β (Aβ) is deposited along the cerebral and meningeal blood vessels, causing an increased incidence of cerebral microbleeds (Yamada, 2000). Aβ also interacts with fibrinogen, the major protein component of blood clots, to induce the oligimerization of fibrinogen, leading to abnormal clot formation (Ahn et al., 2010). The resulting clots are resistant to degradation and confer an increased susceptibility to thrombosis (Cortes-Canteli et al., 2010) and disrupting the interaction between Aβ and fibrinogen appears to partially restore normal thrombosis and delay cognitive decline in mice (Ahn et al., 2014). Thus, CAA and the interaction between fibrinogen and Aβ could be potential additional mechanisms for the hypoperfusion observed in AD mice.

Several previous studies indicate that 5xFAD mice have very rapid disease progression, which is likely more rapid than that of TgCRND8 mice. 5xFAD mice develop extracellular amyloid deposition beginning around 2-month-old age in the subiculum and cortex, which increases rapidly with age and is found throughout the brain by six months (Chen et al., 2019; Oakley et al., 2006). They also show astrogliosis and microgliosis at 2 months of age, indicating that neuroinflammation occurs early in this model (Nakai et al., 2021) and neurodegeneration as early as 4–5 months of age (Hall and Roberson, 2012; Oakley et al., 2006). Our Congo red staining indicated that at 7 and 12 months of age, 5xFAD mice show similar levels of amyloid plaque (supplementary Fig. 2C, D), but 12-month-old 5xFAD mice showed broader diffused plaques which are difficult to quantify. In TgCRND8 mice, astrogliosis can be seen as early as at 3 months (Spanos and Liddelow, 2020) and amyloid deposition starts at 3 months and has densely-cored plaques evident from 5 months of age (Chishti et al., 2001). TgCRND8 mice also show neuro-morphological abnormalities which do not appear until 6 months of age (Hall and Roberson, 2012; Nakai et al., 2021). Furthermore, CAA accumulation could be detected at 3 months of age in 5xFAD (Zenaro et al., 2015), which does not arise in TgCRND8 mice until 6-7 months (Klohs et al., 2014). This could explain accelerated cerebrovascular pathology in this strain, resulting in an earlier onset of VEGF-mediated compensatory mechanisms that are not seen in the more slowly progressive disease of TgCRND8 mice.

In the current studies, there is evidence that increased VEGF/VEGFR expression is associated with increased CBV and restore CBF in AD mice. In previous studies. inhibition and upregulation of VEGF-R2 has shown this receptor to be important to vascularization and pruning, with reduced levels resulting in enhanced capillary recanalization following obstruction (Reeson et al., 2018). Administration of VEGF has been shown to decrease vascular apoptosis and improve behavioral testing in TgCRND8 mice (Religa et al., 2013) and reduced Aβ levels and improved cognition in APP/PS1 mice (Liu et al., 2021). It will be interesting to test whether increasing VEGF levels in TgCRND8 can improves CBF and hypometabolism. Based on the current study, these seemingly paradoxical findings may be related to differences between mouse strains. Therefore, interpretation of current and future results should consider the particular cerebrovascular phenotype of each strain in question.

5. Conclusion

Despite their differences, both mouse strains showed predictable patterns of disease progression that were revealed through *in vivo* imaging. In TgCRND8 mice there is decreasing CBF and cerebral metabolism over time, and in 5xFAD mice, there is a biphasic CBF pattern and an increase in CBV over time. These imaging modalities are therefore potentially valuable for longitudinal monitoring of disease progression in these AD mouse models. In addition, neuroinflammation and VEGF dependent vasodilation can be crucial events which can alter cerebral circulation and metabolism during the progression of AD. It is important, however, to be familiar with the patterns of each particular strain when using imaging modalities to monitor disease progression and investigate molecular mechanisms underlying their phenotypes rather than making assumptions from human findings or those of other strains. Understanding these differences between strains is also important for future studies examining cerebrovascular pathology in AD mouse models.

Disclosure statement

The authors have no conflict of interest to report.

Acknowledgements

The authors would like to thank the Citigroup Biomedical Imaging Center and its members, including Henning Voss, Bin He, and Dohyun Kim for their crucial assistance with imaging studies. We also thank members of the Comparative Bioscience Center at Rockefeller University including Skye Rasmussen and Ravi Tolwani for their crucial support throughout the project. We are grateful to all members of the Strickland Laboratory for their invaluable input. We thank animal care staff at The Rockefeller University and Weill Cornell Medicine, including Craig Hunter and Lisa Eldred for assisting in animal care and providing an ideal environment for our mice. The lead author thanks mentors of the Tri-Institutional Laboratory Animal Medicine Training Program, including Neil Lipman, for their assistance and support throughout the study.

This work was supported by the National Institute of Health NS104386 (Ahn) and NS10668 (Norris and Strickland), Cure Alzheimer's Fund, Alzheimer's Association, Rudin Family Foundation, and John A. Herrmann, Jr. S.A. The authors declare that there is no conflict of interest.

Author contributions

Nicholas M. Tataryna: Methodology, Validation, Formal analysis, Investigation, Writing - original draft, Visualization. **Vishal Singh:** Methodology, Investigation, Writing - review & editing, Visualization. **Jonathan Dyke:** MRI sequences design, Image analysis. **HannaBerk-Rauch:** Methodology, Investigation, **Dana Clausen:** Methodology, Investigation. **Eric Aronowitzd: MRI sequence design, MRI scanning**, **Erin H. Norris:** Methodology, Writing - review & editing. **Sidney Strickl:** Methodology, Writing - review & editing. **Hyung Jin Ahn:** Methodology, Validation, Formal analysis, Investigation, Data curation, Supervision, Writing - review & editing.

Supplementary materials

Supplementary material associated with this article can be found, in the online version, at doi:10.1016/j.neurobiolaging.2021.07.015.

References

Ahn, H.J., Glickman, J.F., Poon, K.L., Zamolodchikov, D., Jno-Charles, O.C., Norris, E.H., Strickland, S., 2014. A novel Abeta-fibrinogen interaction inhibitor rescues altered thrombosis and cognitive decline in Alzheimer's disease mice. J Exp Med 211 (6), 1049–1062.

Ahn, H.J., Zamolodchikov, D., Cortes-Canteli, M., Norris, E.H., Glickman, J.F., Strickland, S., 2010. Alzheimer's disease peptide beta-amyloid interacts with fibrinogen and induces its oligomerization. Proc Natl Acad Sci U S A 107 (50), 21812–21817.

Altmann, A., Ng, B., Landau, S.M., Jagust, W.J., Greicius, M.D.Alzheimer's Disease Neuroimaging, I., 2015. Regional brain hypometabolism is unrelated to regional amyloid plaque burden. Brain 138 (Pt 12), 3734–3746.

Austin, B.P., Nair, V.A., Meier, T.B., Xu, G., Rowley, H.A., Carlsson, C.M., Johnson, S.C., Prabhakaran, V., 2011. Effects of hypoperfusion in Alzheimer's disease. Journal of Alzheimer's disease: JAD (26 Suppl 3) 123–133.

Ben Haim, L., Carrillo-de Sauvage, M.A., Ceyzeriat, K., Escartin, C., 2015. Elusive roles for reactive astrocytes in neurodegenerative diseases. Front Cell Neurosci 9, 278.

Bos, A., Bergmann, R., Strobel, K., Hofheinz, F., Steinbach, J., den Hoff, J., 2012. Cerebral blood flow quantification in the rat: a direct comparison of arterial spin labeling MRI with radioactive microsphere PET. EJNMMI Res 2 (1), 47.

Boxerman, J.L., Schmainda, K.M., Weisskoff, R.M., 2006. Relative cerebral blood volume maps corrected for contrast agent extravasation significantly correlate with glioma tumor grade, whereas uncorrected maps do not. AJNR Am J Neuroradiol 27 (4), 859–867.

Brosch, J.R., Farlow, M.R., Risacher, S.L., Apostolova, L.G., 2017. Tau imaging in Alzheimer's disease diagnosis and clinical trials. Neurotherapeutics 14 (1), 62–68.

Caminiti, S.P., Ballarini, T., Sala, A., Cerami, C., Presotto, L., Santangelo, R., Fallanca, F., Vanoli, E.G., Gianolli, L., Iannaccone, S., Magnani, G., Perani, D., Project, B., 2018. FDG-PET and CSF biomarker accuracy in prediction of conversion to different dementias in a large multicentre MCI cohort. Neuroimage Clin 18, 167–177.

Carmeliet, P., 2005. VEGF as a key mediator of angiogenesis in cancer. Oncology 69 (Suppl 3), 4–10.

Chalmers, K., Wilcock, G.K., Love, S., 2003. APOE epsilon 4 influences the pathological phenotype of Alzheimer's disease by favouring cerebrovascular over parenchymal accumulation of A beta protein. Neuropathol Appl Neurobiol 29 (3), 231–238.

Chandra, A., Valkimadi, P.E., Pagano, G., Cousins, O., Dervenoulas, G., Politis, M.Alzheimer's Disease Neuroimaging, I., 2019. Applications of amyloid, tau, and neuroinflammation PET imaging to Alzheimer's disease and mild cognitive impairment. Hum Brain Mapp 40 (18), 5424–5442.

Chao, L.L., Buckley, S.T., Kornak, J., Schuff, N., Madison, C., Yaffe, K., Miller, B.L., Kramer, J.H., Weiner, M.W., 2010. ASL perfusion MRI predicts cognitive decline and conversion from MCI to dementia. Alzheimer Dis Assoc Disord 24 (1), 19–27.

Chen, Y., Shi, G.W., Liang, Z.M., Sheng, S.Y., Shi, Y.S., Peng, L., Wang, Y.P., Wang, F., Zhang, X.M., 2019. Resveratrol improves cognition and decreases amyloid plaque formation in Tg6799 mice. Mol Med Rep 19 (5), 3783–3790.

Chen, Y., Wolk, D.A., Reddin, J.S., Korczykowski, M., Martinez, P.M., Musiek, E.S., Newberg, A.B., Julin, P., Arnold, S.E., Greenberg, J.H., Detre, J.A., 2011. Voxel-level comparison of arterial spin-labeled perfusion MRI and FDG-PET in Alzheimer disease. Neurology 77 (22), 1977–1985.

Chishti, M.A., Yang, D.S., Janus, C., Phinney, A.L., Horne, P., Pearson, J., Strome, R., Zuker, N., Loukides, J., French, J., Turner, S., Lozza, G., Grilli, M., Kunicki, S., Morissette, C., Paquette, J., Gervais, F., Bergeron, C., Fraser, P.E., Carlson, G.A., George-Hyslop, P.S., Westaway, D., 2001. Early-onset amyloid deposition and cognitive deficits in transgenic mice expressing a double mutant form of amyloid precursor protein 695. J Biol Chem 276 (24), 21562–21570.

Cortes-Canteli, M., Paul, J., Norris, E.H., Bronstein, R., Ahn, H.J., Zamolodchikov, D., Bhuvanendran, S., Fenz, K.M., Strickland, S., 2010. Fibrinogen and beta-amyloid association alters thrombosis and fibrinolysis: a possible contributing factor to Alzheimer's disease. Neuron 66 (5), 695–709.

Creighton, S.D., Mendell, A.L., Palmer, D., Kalisch, B.E., MacLusky, N.J., Prado, V.F., Prado, M.A.M., Winters, B.D., 2019. Dissociable cognitive impairments in two strains of transgenic Alzheimer's disease mice revealed by a battery of object-based tests. Sci Rep 9 (1), 57.

de la Torre, J.C., 2004. Is Alzheimer's disease a neurodegenerative or a vascular disorder? Data, dogma, and dialectics. Lancet Neurol 3 (3), 184–190.

Deleye, S., Waldron, A.M., Richardson, J.C., Schmidt, M., Langlois, X., Stroobants, S., Staelens, S., 2016. The Effects of Physiological and Methodological Determinants on 18F-FDG Mouse Brain Imaging Exemplified in a Double Transgenic Alzheimer Model. Mol Imaging 15.

Du, A.T., Jahng, G.H., Hayasaka, S., Kramer, J.H., Rosen, H.J., Gorno-Tempini, M.L., Rankin, K.P., Miller, B.L., Weiner, M.W., Schuff, N., 2006. Hypoperfusion in frontotemporal dementia and Alzheimer disease by arterial spin labeling MRI. Neurology 67 (7), 1215–1220.

Dubois, A., Herard, A.S., Delatour, B., Hantraye, P., Bonvento, G., Dhenain, M., Delzescaux, T., 2010. Detection by voxel-wise statistical analysis of significant changes in regional cerebral glucose uptake in an APP/PS1 transgenic mouse model of Alzheimer's disease. NeuroImage 51 (2), 586–598.

Ellis, R.J., Olichney, J.M., Thal, L.J., Mirra, S.S., Morris, J.C., Beekly, D., Heyman, A., 1996. Cerebral amyloid angiopathy in the brains of patients with Alzheimer's disease: the CERAD experience. Part XV. Neurol 46 (6), 1592–1596.

Fueger, B.J., Czernin, J., Hildebrandt, I., Tran, C., Halpern, B.S., Stout, D., Phelps, M.E., Weber, W.A., 2006. Impact of animal handling on the results of 18F-FDG PET studies in mice. J Nucl Med 47 (6), 999–1006.

Furst, A.J., Rabinovici, G.D., Rostomian, A.H., Steed, T., Alkalay, A., Racine, C., Miller, B.L., Jagust, W.J., 2012. Cognition, glucose metabolism and amyloid burden in Alzheimer's disease. Neurobiol Aging 33 (2), 215–225.

Garibotto, V., Herholz, K., Boccardi, M., Picco, A., Varrone, A., Nordberg, A., Nobili, F., Ratib, O.Geneva Task Force for the Roadmap of Alzheimer's, B., 2017. Clinical validity of brain fluorodeoxyglucose positron emission tomography as a biomarker for Alzheimer's disease in the context of a structured 5-phase development framework. Neurobiol Aging 52, 183–195.

Girouard, H., Iadecola, C., 2006. Neurovascular coupling in the normal brain and in hypertension, stroke, and Alzheimer disease. J Appl Physiol 100 (1), 328–335.

Hall, A.M., Roberson, E.D., 2012. Mouse models of Alzheimer's disease. Brain Res Bull 88 (1), 3–12.

Hebert, F., Grand'maison, M., Ho, M.K., Lerch, J.P., Hamel, E., Bedell, B.J., 2013. Cortical atrophy and hypoperfusion in a transgenic mouse model of Alzheimer's disease. Neurobiol Aging 34 (6), 1644–1652.

Hemonnot, A.L., Hua, J., Ulmann, L., Hirbec, H., 2019. Microglia in Alzheimer disease: well-known targets and new opportunities. Front Aging Neurosci 11, 233.

Herholz, K., Westwood, S., Haense, C., Dunn, G., 2011. Evaluation of a calibrated (18)F-FDG PET score as a biomarker for progression in Alzheimer disease and mild cognitive impairment. J Nucl Med 52 (8), 1218–1226.

Herscovitch, P., Raichle, M.E., 1985. What is the correct value for the brain blood partition-coefficient for water. J Cerebr Blood F Met 5 (1), 65–69.

Iadecola, C., 2004. Neurovascular regulation in the normal brain and in Alzheimer's disease. Nat Rev Neurosci 5 (5), 347–360.

Kato, T., Inui, Y., Nakamura, A., Ito, K., 2016. Brain fluorodeoxyglucose (FDG) PET in dementia. Ageing Res Rev 30, 73–84.

Kim, S.G., 1995a. Quantification of relative cerebral blood-flow change by flow-sensitive alternating inversion-recovery (fair) technique - application to functional mapping. Magnet Reson Med 34 (3), 293–301.

Kim, S.G., 1995b. Quantification of relative cerebral blood flow change by flow-sensitive alternating inversion recovery (FAIR) technique: application to functional mapping. Magn Reson Med 34 (3), 293–301.

Klohs, J., Rudin, M., Shimshek, D.R., Beckmann, N., 2014. Imaging of cerebrovascular pathology in animal models of Alzheimer's disease. Front Aging Neurosci 6, 32.

Kober, F., Iltis, I., Izquierdo, M., Desrois, M., Ibarrola, D., Cozzone, P.J., Bernard, M., 2004. High-resolution myocardial perfusion mapping in small animals in vivo by spin-labeling gradient-echo imaging. Magn Reson Med 51 (1), 62–67.

Korte, N., Nortley, R., Attwell, D., 2020. Cerebral blood flow decrease as an early pathological mechanism in Alzheimer's disease. Acta neuropathologica 140 (6), 793–810.

Ku, D.D., Zaleski, J.K., Liu, S., Brock, T.A., 1993. Vascular endothelial growth factor induces EDRF-dependent relaxation in coronary arteries. Am J Physiol 265 (2 Pt 2), H586–H592.

Lee S. van der, A.B.L.M., 1956. Acta Physiol Pharmacol Neer 5, 213.

Liu, M.H., Jin, H.K., Floten, H.S., Yang, Q., Yim, A.P., Furnary, A., Zioncheck, T.F., Bunting, S., He, G.W., 2001. Vascular endothelial growth factor-mediated endothelium-dependent relaxation is blunted in spontaneously hypertensive rats. J Pharmacol Exp Ther 296 (2), 473–477.

Liu, X., Chu, B., Jin, S., Li, M., Xu, Y., Yang, H., Feng, Z., Bi, J., Wang, P., 2021. Vascular endothelial growth factor alleviates mitochondrial dysfunction and suppression of mitochondrial biogenesis in models of Alzheimer's disease. Int J Neurosci 131 (2), 154–162.

Luo, F., Rustay, N.R., Ebert, U., Hradil, V.P., Cole, T.B., Llano, D.A., Mudd, S.R., Zhang, Y., Fox, G.B., Day, M., 2012. Characterization of 7- and 19-month-old Tg2576 mice using multimodal in vivo imaging: limitations as a translatable model of Alzheimer's disease. Neurobiol Aging 33 (5), 933–944.

Macdonald, I.R., DeBay, D.R., Reid, G.A., O'Leary, T.P., Jollymore, C.T., Mawko, G., Burrell, S., Martin, E., Bowen, C.V., Brown, R.E., Darvesh, S., 2014. Early detection of cerebral glucose uptake changes in the 5XFAD mouse. Curr Alzheimer Res. 11 (5), 450–460.

Mahoney, E.R., Dumitrescu, L., Moore, A.M., Cambronero, F.E., De Jager, P.L., Koran, M.E.I., Petyuk, V.A., Robinson, R.A.S., Goyal, S., Schneider, J.A., Bennett, D.A., Jefferson, A.L., Hohman, T.J., 2021. Brain expression of the vascular endothelial growth factor gene family in cognitive aging and alzheimer's disease. Mol Psychiatry 26 (3), 888–896.

Maia Jr., A.C., Malheiros, S.M., da Rocha, A.J., da Silva, C.J., Gabbai, A.A., Ferraz, F.A., Stavale, J.N., 2005. MR cerebral blood volume maps correlated with vascular endothelial growth factor expression and tumor grade in nonenhancing gliomas. AJNR Am J Neuroradiol. 26 (4), 777–783.

Mandrekar-Colucci, S., Landreth, G.E., 2010. Microglia and inflammation in Alzheimer's disease. CNS Neurol Disord Drug Targets. 9 (2), 156–167.

Maynard, S.E., Min, J.Y., Merchan, J., Lim, K.H., Li, J., Mondal, S., Libermann, T.A., Morgan, J.P., Sellke, F.W., Stillman, I.E., Epstein, F.H., Sukhatme, V.P., Karumanchi, S.A., 2003. Excess placental soluble fms-like tyrosine kinase 1 (sFlt1) may contribute to endothelial dysfunction, hypertension, and proteinuria in preeclampsia. J Clin Invest 111 (5), 649–658.

Montagne, A., Nation, D.A., Pa, J., Sweeney, M.D., Toga, A.W., Zlokovic, B.V., 2016. Brain imaging of neurovascular dysfunction in Alzheimer's disease. Acta Neuropathol. 131 (5), 687–707.

Mosconi, L., Berti, V., Glodzik, L., Pupi, A., De Santi, S., de Leon, M.J., 2010. Pre-clinical detection of Alzheimer's disease using FDG-PET, with or without amyloid imaging. J Alzheimer's Dis 20 (3), 843–854.

Nakai, T., Yamada, K., Mizoguchi, H., 2021. Alzheimer's disease animal models: elucidation of biomarkers and therapeutic approaches for cognitive impairment. Int J Mol Sci 22 (11).

Ng, K.P., Pascoal, T.A., Mathotaarachchi, S., Chung, C.O., Benedet, A.L., Shin, M., Kang, M.S., Li, X., Ba, M., Kandiah, N., Rosa-Neto, P., Gauthier, S.Alzheimer's Disease Neuroimaging, I., 2017. Neuropsychiatric symptoms predict hypometabolism in preclinical Alzheimer disease. Neurology 88 (19), 1814–1821.

Ni, Y., May, V., Braas, K., Osol, G., 1997. Pregnancy augments uteroplacental vascular endothelial growth factor gene expression and vasodilator effects. Am J Physiol 273 (2 Pt 2), H938–H944.

Oakley, H., Cole, S.L., Logan, S., Maus, E., Shao, P., Craft, J., Guillozet-Bongaarts, A., Ohno, M., Disterhoft, J., Van Eldik, L., Berry, R., Vassar, R., 2006. Intraneuronal beta-amyloid aggregates, neurodegeneration, and neuron loss in transgenic mice with five familial Alzheimer's disease mutations: potential factors in amyloid plaque formation. J Neurosci 26 (40), 10129–10140.

Ostergaard, L., Aamand, R., Gutierrez-Jimenez, E., Ho, Y.C., Blicher, J.U., Madsen, S.M., Nagenthiraja, K., Dalby, R.B., Drasbek, K.R., Moller, A., Braendgaard, H., Mouridsen, K., Jespersen, S.N., Jensen, M.S., West, M.J., 2013. The capillary dysfunction hypothesis of Alzheimer's disease. Neurobiol Aging 34 (4), 1018–1031.

Paxinos, G., Franklin, K.B.J., 2004. The mouse brain in stereotaxic coordinates, Compact, 2nd ed. Elsevier Academic Press, Amsterdam; Boston.

Petcharunpaisan, S., Ramalho, J., Castillo, M., 2010. Arterial spin labeling in neuroimaging. World J Radiol 2 (10), 384–398.

Reeson, P., Choi, K., Brown, C.E., 2018. VEGF signaling regulates the fate of obstructed capillaries in mouse cortex. Elife 7, e33670. doi:10.7554/eLife.33670.

Religa, P., Cao, R., Religa, D., Xue, Y., Bogdanovic, N., Westaway, D., Marti, H.H., Winblad, B., Cao, Y., 2013. VEGF significantly restores impaired memory behavior in Alzheimer's mice by improvement of vascular survival. Sci Rep 3, 2053.

Rice, L., Bisdas, S., 2017. The diagnostic value of FDG and amyloid PET in Alzheimer's disease-A systematic review. Eur J Radiol 94, 16–24.

Rissanen, T.T., Korpisalo, P., Markkanen, J.E., Liimatainen, T., Orden, M.R., Kholova, I., de Goede, A., Heikura, T., Grohn, O.H., Yla-Herttuala, S., 2005. Blood flow remodels growing vasculature during vascular endothelial growth factor gene therapy and determines between capillary arterialization and sprouting angiogenesis. Circulation 112 (25), 3937–3946.

Rojas, S., Herance, J.R., Gispert, J.D., Abad, S., Torrent, E., Jimenez, X., Pareto, D., Perpina, U., Sarroca, S., Rodriguez, E., Ortega-Aznar, A., Sanfeliu, C., 2013. In vivo evaluation of amyloid deposition and brain glucose metabolism of 5XFAD mice using positron emission tomography. Neurobiol Aging 34 (7), 1790–1798.

Ryu, J.K., McLarnon, J.G., 2008. VEGF receptor antagonist Cyclo-VEGI reduces inflammatory reactivity and vascular leakiness and is neuroprotective against acute excitotoxic striatal insult. J Neuroinflammation 5, 18.

Sarikaya, I., 2015. PET imaging in neurology: Alzheimer's and Parkinson's diseases. Nuclear Med Commun 36 (8), 775–781.

Sierra-Marcos, A., 2017. Regional cerebral blood flow in mild cognitive impairment and alzheimer's disease measured with arterial spin labeling magnetic resonance imaging. Int J Alzheimer's Dis 2017, 5479597.

Spanos, F., Liddelow, S.A., 2020. An overview of astrocyte responses in genetically induced Alzheimer's disease mouse models. Cells 9 (11), 2415.

Van Vickle, G.D., Esh, C.L., Kalback, W.M., Patton, R.L., Luehrs, D.C., Kokjohn, T.A., Fifield, F.G., Fraser, P.E., Westaway, D., McLaurin, J., Lopez, J., Brune, D., Newel, A.J., Poston, M., Beach, T.G., Roher, A.E., 2007. TgCRND8 amyloid precursor protein transgenic mice exhibit an altered gamma-secretase processing and an aggressive, additive amyloid pathology subject to immunotherapeutic modulation. Biochemistry 46 (36), 10317–10327.

Viswanathan, A., Rocca, W.A., Tzourio, C., 2009. Vascular risk factors and dementia: how to move forward? Neurology 72 (4), 368–374.

Waldron, A.M., Wintmolders, C., Bottelbergs, A., Kelley, J.B., Schmidt, M.E., Stroobants, S., Langlois, X., Staelens, S., 2015. In vivo molecular neuroimaging of glucose utilization and its association with fibrillar amyloid-beta load in aged APPPS1-21 mice. Alzheimer's Res Ther 7 (1), 76.

Xiao, N.A., Zhang, J., Zhou, M., Wei, Z., Wu, X.L., Dai, X.M., Zhu, Y.G., Chen, X.C., 2015. Reduction of glucose metabolism in olfactory bulb is an earlier alzheimer's disease-related biomarker in 5XFAD Mice. Chinese Med J 128 (16), 2220–2227.

Yamada, M., 2000. Cerebral amyloid angiopathy: an overview. Neuropathology 20 (1), 8–22.

Zenaro, E., Pietronigro, E., Della Bianca, V., Piacentino, G., Marongiu, L., Budui, S., Turano, E., Rossi, B., Angiari, S., Dusi, S., Montresor, A., Carlucci, T., Nani, S., Tosadori, G., Calciano, L., Catalucci, D., Berton, G., Bonetti, B., Constantin, G., 2015. Neutrophils promote Alzheimer's disease-like pathology and cognitive decline via LFA-1 integrin. Nat Med 21 (8), 880–886.

Zlokovic, B.V., 2011. Neurovascular pathways to neurodegeneration in Alzheimer's disease and other disorders. Nat Rev Neurosci 12 (12), 723–738.